

Unraveling the Nature of Magnetism of the $5d^4$ Double Perovskite Ba_2YIrO_6

S. Fuchs,^{1,2} T. Dey,¹ G. Aslan-Cansever,^{1,3} A. Maljuk,¹ S. Wurmehl,¹ B. Büchner,^{1,2} and V. Kataev¹

¹Leibniz Institute for Solid State and Materials Research IFW Dresden, D-01171 Dresden, Germany

²Institut für Festkörper- und Materialphysik, Technische Universität Dresden, D-01062 Dresden, Germany

³Institut für Festkörper- und Materialphysik, Technische Universität Dresden, 01062 Dresden, Germany

We report electron spin resonance (ESR) spectroscopy results on the double perovskite Ba_2YIrO_6 . On general grounds, this material is expected to be nonmagnetic due to the strong coupling of the spin and orbital momenta of Ir^{5+} ($5d^4$) ions. However, controversial experimental reports on either strong antiferromagnetism with static order at low temperatures or just a weakly paramagnetic behavior have triggered a discussion on the breakdown of the generally accepted scenario of the strongly spin-orbit coupled ground states in the $5d^4$ iridates and the emergence of a novel exotic magnetic state. Our data evidence that the magnetism of the studied material is solely due to a few percent of Ir^{4+} and Ir^{6+} magnetic defects while the regular Ir^{5+} sites remain nonmagnetic. Remarkably, the defect Ir^{6+} species manifest magnetic correlations in the ESR spectra at $T \lesssim 20$ K suggesting a long-range character of superexchange in the double perovskites as proposed by recent theories.

PACS numbers: 76.30.-v, 76.30.He, 71.70.Ch, 71.70.Ej, 75.50.Ee

Keywords: iridates, spin-orbit coupling, magnetism, electron spin resonance

Introduction.— Complex iridium oxides are attracting since about 10 years unceasingly large interest in the condensed matter community worldwide due to predictions of exotic ground states in these materials, such as a spin-orbit assisted Mott insulating state, quantum spin liquid phases, Weyl semimetallic behavior, and superconductivity (for reviews see, e.g., [1–5]). Such a rich behavior is expected in iridates due to comparable energy scales of spin-orbit coupling (SOC), electronic bandwidths, non-cubic crystal fields and local Coulomb interactions U .

In the widely studied Ir-based compounds, such as, e.g., layered perovskites Sr_2IrO_4 [6] and $\text{Sr}_3\text{Ir}_2\text{O}_7$ [7], honeycomb compounds Na_2IrO_3 [8], $\alpha\text{-Li}_2\text{IrO}_3$ [9] and their three-dimensional analogues β - and $\gamma\text{-Li}_2\text{IrO}_3$ [10–12], hyperkagome compound $\text{Na}_4\text{Ir}_3\text{O}_8$ [13] and several other materials, the carrier of magnetic moments are Ir^{4+} ($5d^5$) ions. Owing to the strong SOC, the spin (S) and orbital (L) momenta are entangled in Ir^{4+} giving rise to the magnetic Kramers doublet characterized by the effective spin $j_{\text{eff}} = 1/2$ [14]. The complex structure of $j_{\text{eff}} = 1/2$ states is in the core of theoretical models predicting exotic magnetic behavior of iridates [15, 16]. In contrast, in the case of Ir^{5+} ($5d^4$) the $S - L$ coupling should yield a singlet ground state with the total angular momentum $J = 0$, whereas the magnetic $J = 1$ triplet lies much higher in energy [17] rendering Ir^{5+} -based iridates nonmagnetic. In this respect, Ir^{5+} double-perovskite iridates Sr_2YIrO_6 , Ba_2YIrO_6 , and their solid solutions have received recently a great deal of interest due to controversial reports on the observation of either strongly antiferromagnetic behavior with static magnetic order at a low temperature [18, 19] or only a weak paramagnetism [20–25]. This has triggered in turn a substantial number of theoretical works developing various scenarios of the breakdown of the j_{eff} description in $4d^4$ and $5d^4$ Mott insulators and its possible relevance to the Ir^{5+} double-

perovskite iridates [26–31], in particular, with regard to the proposed mechanism of condensation of $J = 1$ excitons [17].

In most of the experimental works magnetic properties of $(\text{Ba,Sr})_2\text{YIrO}_6$ were characterized by bulk static magnetometry and specific heat measurements which enabled one to estimate the average magnetic moment, the average magnetic exchange coupling strength and to detect a possible transition to the magnetically ordered state. However, considering the controversy of experimental results and theoretical predictions, it is of paramount importance to identify the exact origin of magnetic behavior and to consolidate experimental results with existing theories.

In this Letter, we report the results of such identification by means of multifrequency electron spin resonance (ESR) spectroscopy. A decisive advantage of ESR is the possibility to separate different contributions to the total static magnetization, to study the dynamics and correlations of different spin species, to determine their spin multiplicity, and to measure their intrinsic spin susceptibility. The sample used in our ESR study was an assembly of small single crystals of Ba_2YIrO_6 characterized structurally and magnetically in Ref. [21]. It shows a weak magnetic response in the static susceptibility corresponding to the average effective moment $\mu_{\text{eff}} = 0.44\mu_{\text{B}}/\text{Ir}$ with no signatures of magnetic order down to 0.4 K. A rich ESR spectrum comprising several lines was observed. A careful analysis of the frequency- and temperature-dependent ESR data yields several important findings: (i) the total concentration of magnetic centers contributing to ESR signals amounts to $\sim 4\%$ of all Ir ions; (ii) the major part of them can be unambiguously identified with Ir^{4+} ($5d^5$) and Ir^{6+} ($5d^3$) magnetic ions. In particular, Ir^{6+} spin-only centers with $S = 3/2$ show a typical triplet fine structure in the ESR

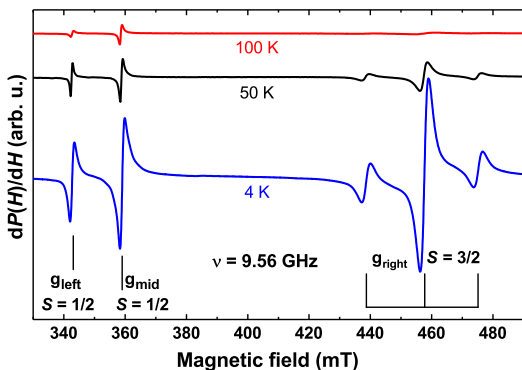


FIG. 1. ESR spectra (field derivatives of absorption) at the X-band frequency $\nu = 9.56$ GHz at three selected temperatures. The lines at ~ 340 mT and ~ 360 mT, and a triplet structure centered around ~ 460 mT are labeled as g_{left} , g_{mid} , and g_{right} , respectively, with the spin values assigned to each line.

spectrum and a characteristic shift of the spectroscopic g factor; (iv) Ir^{6+} spin centers exhibit correlated behavior below ~ 20 K. This enables a definitive conclusion that the magnetism of Ba_2YIrO_6 is not related to the conjectured breakdown of the $J = 0$ state of the regular Ir^{5+} ($5d^4$) lattice in this material and the occurrence of a weak magnetic moment on every Ir^{5+} ($5d^4$) site but is rather due to different kinds of interacting paramagnetic defects which could even order magnetically at a low temperature if their concentration exceeds a certain threshold level.

Results.— Representative ESR spectra of Ba_2YIrO_6 at different temperatures measured at frequency $\nu = 9.56$ GHz with a Bruker EMX X-band spectrometer are presented in Fig. 1. Each spectrum comprises a set of sharp resonance lines in the field range 0.33 – 0.49 T. The triplet set of lines at the high field side is composed of the main peak at a resonance field $\mu_0 H_{\text{res}} = 458$ mT, which is accompanied by two satellites at the left and right sides of the main peak. At the low field side, there are two lines at $\mu_0 H_{\text{res}} = 343$ mT and 359 mT. Assuming the simple paramagnetic ESR resonance condition $h\nu = g\mu_B\mu_0 H_{\text{res}}$ one obtains the effective g factors for the left, middle, and high field side peaks of $g_{\text{left}} = 2.00$, $g_{\text{mid}} = 1.90$ and $g_{\text{right}} = 1.49$, respectively. Here h is the Planck constant, μ_B is the Bohr magneton, and μ_0 is the vacuum permeability.

The single lines g_{left} and g_{mid} in the ESR spectrum can be straightforwardly assigned to magnetic species carrying the spin $S = 1/2$. To identify the spin centers giving rise to the triplet structure around 460 mT ESR measurements at higher excitation frequencies have been performed with a homemade spectrometer [32] equipped with the PNA-X network analyzer from Keysight Technology and a 16 T superconducting magnet system from Oxford Instruments. In Fig. 2, the $\nu - H_{\text{res}}$ diagram of the resonance modes is shown. The resonance branches

$\nu(H_{\text{res}})$ are linear in field. Their slopes $\partial\nu/\partial H$ yield the g factors that nicely agree with the result obtained at $\nu = 9.56$ GHz. As the g values for the three main lines are different, the spacing between the lines in the spectrum progressively increases with increasing ν . Remarkably, this is not the case for the satellites of the g_{right} peak. Being resolved at ~ 10 GHz, at higher frequencies they remain hidden under the broadened main peak, suggesting that this group of lines is characterized by the same g factor $g_{\text{right}} = 1.49$. Such a triplet structure typically arises from magnetic species carrying spin $S = 3/2$. In a solid, the $(2S + 1)$ -fold degeneracy of the spin levels can be partially lifted in a zero magnetic field due to a combined action of the crystal field (CF) and the spin-orbit coupling. The splitting of these levels giving rise to a fine structure of the ESR signal can be described by the Hamiltonian [33]

$$\mathcal{H} = \mu_B \vec{S} \cdot \mathbf{g} \cdot \vec{H} + \vec{S} \cdot \mathbf{D} \cdot \vec{S}. \quad (1)$$

Here, the first and second terms account for the Zeeman interaction with the magnetic field and the interaction with the crystal field, respectively. In a simple case of uniaxial symmetry, the CF tensor \mathbf{D} reduces to a scalar, and the second term of (1) simplifies to

$$\vec{S} \cdot \mathbf{D} \cdot \vec{S} = D [S_z^2 - S(S + 1)/3]. \quad (2)$$

It follows from (2) that the Kramers doublets $|\pm 1/2\rangle$ and $|\pm 3/2\rangle$ of the $S = 3/2$ spin multiplet are separated in energy by $2D$. This gives rise to a “fine-structure” of the ESR spectrum consisting of the main peak due to the resonance transition $|+1/2\rangle \leftrightarrow |-1/2\rangle$ and two weaker in intensity satellites $|\pm 1/2\rangle \leftrightarrow |\pm 3/2\rangle$ with a frequency-independent offset $\pm D$ from the central line.

Since the integrated intensity of an ESR signal I^{ESR} is proportional to the static susceptibility χ of the resonating spins [33], it can be compared with the bulk susceptibility measurements (Fig. 3). The T dependence of the total intensity $I_{\text{tot}}^{\text{ESR}}$ of all lines in the ESR spectrum of Ba_2YIrO_6 agrees very well with the static magnetic data $\chi(T)$ [Fig. 3(a)], suggesting that the same spins are probed by ESR and static magnetic measurements. In particular, $I_{\text{tot}}^{\text{ESR}}$ follows the Curie-Weiss law at higher temperatures and, similar to $\chi(T)$, deviates from it below $T \sim 15 - 20$ K signaling the onset of the correlated regime for the resonating spins. The signal g_{right} makes the major contribution to $I_{\text{tot}}^{\text{ESR}}$ of $\sim 73\%$, whereas signals g_{left} and g_{mid} contribute to a much lesser extent (see Table I). To estimate the absolute concentration n_i of the spins contributing to the respective signals their intensities were calibrated against a reference sample, a single crystal of Al_2O_3 doped with a well-defined, small concentration of Cr^{3+} ions (for details, see Refs. [34, 35]). The analysis (summarized in Table I) reveals the total concentration of spins $\sum_i n_i$ contributing to the ESR spectrum of about 4 % per unit cell of Ba_2YIrO_6 . This value is sim-

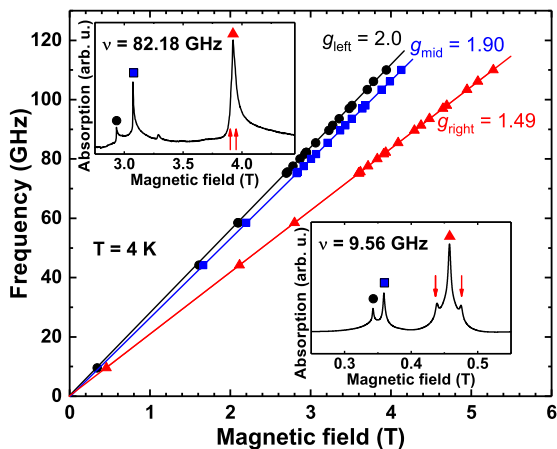


FIG. 2. Frequency ν vs resonance field H_{res} dependence of the peaks in the ESR spectrum (data points). Solid lines are fits to the relation $h\nu = g\mu_B\mu_0 H_{\text{res}}$ yielding the g factor values as indicated in the plot. The insets show spectra at two selected frequencies. The spectrum at 9.56 GHz was obtained by integration of the absorption derivative spectrum (cf. Fig. 1). Arrows in the upper inset indicate the expected positions of the satellites of the g_{right} peak in the spectrum at 82.18 GHz which are resolved at 9.5 GHz (lower inset).

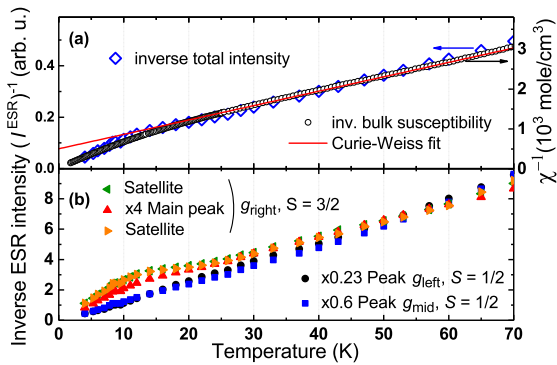


FIG. 3. T dependence of the inverse ESR intensity $1/I_i^{\text{ESR}}$ at $\nu = 9.56$ GHz and its comparison with the static bulk susceptibility χ : (a) total ESR intensity (diamonds, left scale), bulk susceptibility (circles, right scale), and its Curie-Weiss fit $\chi^{-1} = [\chi_0 + C/(T - \theta_{\text{CW}})]^{-1}$ with the antiferromagnetic Curie-Weiss temperature $\theta_{\text{CW}} = -16$ K and the Curie constant $C = 0.0294 \text{ cm}^3\text{K/mol}$ corresponding to the effective magnetic moment $\mu_{\text{eff}} = 0.48\mu_B/\text{Ir}$ (solid line, right scale); (b) intensities of individual lines $1/I_i^{\text{ESR}}$. For better comparison, the data are scaled as indicated in the legend.

ilar to the spin concentration evaluated from the analysis of the static magnetic data [21].

As can be concluded from the comparison of Figs. 3(a) and (b) the $S = 3/2$ centers which give rise to the ESR signal g_{right} are mainly responsible for the deviation of the spin susceptibility from the paramagnetic Curie-Weiss dependence at low temperatures, have the largest Curie-Weiss temperature θ_{CW} (Table I), and, thus, are "more correlated" than other spin species contributing to

TABLE I. Parameters of the lines in the ESR spectrum of Ba_2YIrO_6 : g factor, spin value S , Curie-Weiss temperature obtained from ESR intensities of individual lines θ_{CW} , relative spectral weights of the signals I_i^{ESR} , absolute concentration of spins per unit cell n_i , and the orbital reduction factor k .

Signal	g factor	S	θ_{CW} (K)	$I_i^{\text{ESR}}/I_{\text{tot}}^{\text{ESR}}$ (%)	n_i	k
g_{left}	2.00	1/2	~ -2	~ 7	~ 0.6	1
g_{mid}	1.90	1/2	~ -2	~ 20	~ 1.7	0.93
g_{right}	1.49	3/2	~ -10	~ 73	~ 1.9	0.4

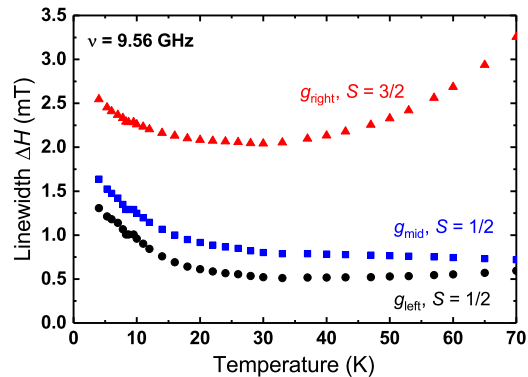


FIG. 4. T dependence of the width ΔH of the ESR signals g_{left} , g_{mid} and g_{right} (main peak) at $\nu = 9.56$ GHz.

the signals g_{left} and g_{mid} . Additional evidence for magnetic correlations at low T comes from the temperature dependence of the ESR linewidth ΔH . Concomitantly with the deviation of $\chi(T)$ from the Curie-Weiss law the linewidth begins to grow below ~ 20 K, indicating the onset of the critical regime characterized by the slowing down of the timescale of spin-spin correlations and a growth of their spatial extension [36]. At higher T , ΔH becomes constant for g_{left} and g_{mid} lines, which is typical for $S = 1/2$ systems with the dominant Heisenberg isotropic exchange interaction in the noncritical regime [36]. Interestingly, for the g_{right} line, ΔH starts to increase above ~ 35 K again, which is indeed characteristic for $S = 3/2$ systems where the phonon modulation of the crystal field potential gives rise to a T -dependent spin-lattice relaxation at elevated temperatures [37].

Discussion.— The small number of magnetic centers contributing to the static magnetization and to ESR spectra of the studied samples of Ba_2YIrO_6 enable a conclusion that the majority of Ir^{5+} ($5d^4$) ions in this compound is in the expected nonmagnetic $J = 0$ state. Thus, the observed magnetic response can be due to the defect Ir sites in the structure with possibly different valences which are likely to occur in a real material. In this respect particular striking is the observation of the $S = 3/2$ centers. Among common oxidation states of Ir, only Ir^{6+} ($5d^3$) has such a spin value. Three $5d$ electrons

evenly occupy three orbitals of the t_{2g} set rendering Ir^{6+} a spin-only $S = 3/2$ ion with no orbital momentum in first order. A classical example of the fine-structure triplet ESR spectrum of an $S = 3/2$ paramagnetic center is the ESR response of $\text{Cr}^{3+}(3d^3)$ ions in a octahedral ligand coordination [33]. It is characterized by a g factor very close to the spin-only value $g_s = 2$ due to the absence of the orbital contribution. A small negative shift ~ -0.05 from g_s due to the second-order spin-orbit coupling effect is parametrized in the perturbation theory as [33]

$$g_{\parallel} \approx g_{\perp} = 2 - 8k\lambda/\Delta. \quad (3)$$

Here, indexes \parallel and \perp denote parallel and perpendicular orientation, respectively, of the applied magnetic field with respect to the symmetry axis of the octahedron, λ is the SOC constant, Δ is the energy difference between the t_{2g} and e_g sets of orbitals, and $k \leq 1$ is the so-called orbital reduction factor which accounts for the covalent character of the metal-ligand bonds ($k = 1$ for ionic bond). A substantially larger negative g shift of -0.51 of the g_{right} signal can be consistently explained by a combined effect of a much stronger spin-orbit coupling in $5d$ Ir as compared to a $3d$ ion and the counteracting effect of the strongly covalent character of Ir - O bonds of the highly oxidized Ir^{6+} [38]. Indeed, with $\lambda \approx 0.5 \text{ eV}$ [39], $\Delta \approx 3.2 \text{ eV}$ [38], and $g_{\text{right}} = 1.49$, one obtains from (3) a rather small value of $k = 0.4$ as is generally expected for $5d$ elements in a high oxidation state (see, e.g., [40–42]).

The $S = 1/2$ ESR line g_{mid} is characterized by a smaller but still a significant negative shift of the g factor from $g_s = 2$. This signal can be assigned to $\text{Ir}^{4+}(5d^5)$ centers with the effective spin $j_{\text{eff}} = 1/2$ covalently bonded with the ligands. Since the spin and orbital momenta are entangled in the Ir^{4+} iridates [14], the g factor is generally anisotropic if the ligand coordination deviates from an ideal octahedral symmetry [33, 43]:

$$\begin{aligned} g_{\parallel} &= (g_s + 2k) \cos^2 \alpha - g_s \sin^2 \alpha; \\ g_{\perp} &= \sqrt{2}k \sin 2\alpha + g_s \sin^2 \alpha; \quad \tan 2\alpha = (2\sqrt{2}\lambda)/(\lambda - 2\delta). \end{aligned} \quad (4)$$

Here, δ is the energy difference between (xz, yz) and xy orbitals of the t_{2g} set arising due to uniaxial distortion. For small distortions $\delta \ll \lambda$, $g_{\parallel} \approx g_{\perp} \approx (g_s + 4k)/3$. With $g_{\text{mid}} = 1.9$, one obtains $k = 0.93$. The larger value of k as compared to the ESR line g_{right} is fully consistent with the expected smaller covalency of the Ir^{4+} -O bond due to a lower oxidation state of the metal ion [38]. Similar results were reported for Ir^{4+} centers in other hosts with nearly cubic local symmetry [44, 45]. Finally, the smallest in intensity ESR signal $g_{\text{left}} = g_s = 2.0$ presumably arises from some $S = 1/2$ defect centers without sizable covalency effects ($k = 1$). Given a very small concentration of $\sim 0.6\%$ of these spin species (Table I), they could be tentatively assigned to stable radical centers localized

at structural imperfections often found in oxide materials (see, e.g., [46]). Both g_{left} and g_{mid} centers carrying a small spin $S = 1/2$ can be considered as the spin probes sensitive to magnetic correlations in the subsystem of the interacting $\text{Ir}^{6+} S = 3/2$ sites in Ba_2YIrO_6 . This explains pronounced low- T upturns of the linewidths of the g_{left} and g_{mid} signals (Fig. 4) most likely arising due to inhomogeneous quasistatic local fields developing in the $S = 3/2$ correlated network below $\sim 15 - 20 \text{ K}$. Here one can trace an analogy with an inhomogeneous broadening of a nuclear magnetic resonance signal of a magnetic solid due to the enhancement of electron spin correlations (see, e.g., [47]).

The exact reasons for the occurrence of $\text{Ir}^{6+} S = 3/2$ centers that appear to be mainly responsible for the unexpected correlated magnetism of Ba_2YIrO_6 have yet to be elucidated. Since the partial concentrations n_i of g_{mid} and g_{right} centers are close (Table I), one thinkable scenario could be a partial static charge disproportionation $\text{Ir}^{5+} \Rightarrow \text{Ir}^{4+} + \text{Ir}^{6+}$. Indeed, since the ESR intensity is proportional to the square of the effective moments of the spins contributing to a given resonance line $I^{\text{ESR}} \sim \mu_{\text{eff}}^2 = g^2 S(S+1) \mu_B^2$ [33], then with g factors from Table I one obtains the ratio $I^{\text{ESR}}(\text{Ir}^{6+}, S = 3/2)/I^{\text{ESR}}(\text{Ir}^{4+}, j_{\text{eff}} = 1/2) = 3.1$, which is close to the intensity ratio of the g_{mid} and the g_{right} signals of 3.65 (Table I). Additionally, Ir^{6+} sites could probably arise due to oxygen excess and/or Ba deficiency. The fact that, despite a relatively small concentration of Ir-related defects, they exhibit spin-correlated behavior below $\sim 20 \text{ K}$ implies significance of long superexchange paths involving several oxygen bridges. This supports theoretical scenarios of the long-range character of magnetic interactions in the $5d$ double perovskites [48, 49] with the active role of nonmagnetic cations, such as Y^{3+} , as mediators of exchange [49]. Furthermore, if to consider the antisite $\text{Y} \leftrightarrow \text{Ir}$ disorder found in Ba_2YIrO_6 [23], the Ir-related defect spin centers might occur also at the Y site. In this situation, as our numerical simulations show [50], magnetic defects even in a moderate concentration of $\sim 5 - 8\%$ could form extended correlated clusters.

Conclusions. – Our multifrequency ESR experiments on the pentavalent iridium double perovskite Ba_2YIrO_6 reveal different paramagnetic centers with the total concentration of $\sim 4\%$ and completely explain the overall static magnetic response. The major contribution can be unambiguously assigned to the defect $\text{Ir}^{6+} S = 3/2$ sites which show clear signatures of magnetic interaction at temperatures below $\sim 20 \text{ K}$. These experimental results give evidence that the regular $\text{Ir}^{5+}(5d^4)$ ions remain in the nonmagnetic $J = 0$ state in Ba_2YIrO_6 , which questions, in general, the scenario of the breakdown of the spin-orbit coupled j_{eff} states in the $5d^4$ double perovskite iridates and the occurrence of a weak magnetic moment on every $\text{Ir}^{5+}(5d^4)$ site. In turn, our findings highlight the relevance of the long-range magnetic interactions in

5d double perovskites proposed in recent theoretical models which might be even responsible for the magnetic order of defect Ir-based spin centers in Ba_2YIrO_6 if their concentration exceeds a certain threshold value.

This work was supported by the Deutsche Forschungsgemeinschaft (DFG) through Grant No. KA 1694/8-1, SFB 1143 (Project B01), and Emmy Noether Grant No. WU 595/3-3.

-
- [1] G. Cao and L. E. DeLong, *Frontiers of 4d- and 5d-Transition Metal Oxides* (World Scientific, Singapore, 2013).
- [2] W. Witzczak-Krempa, G. Chen, Y. B. Kim, and L. Balents, *Annu. Rev. Condens. Matter Phys.* **5**, 57 (2014).
- [3] J. G. Rau, E. K.-H. Lee, and H.-Y. Kee, *Annu. Rev. Condens. Matter Phys.* **7**, 195 (2016).
- [4] S. M. Winter, A. A. Tsirlin, M. Daghofer, J. van den Brink, Y. Singh, P. Gegenwart, and R. Valentí, *J. Phys: Condense Matter* **29**, 493002 (2017).
- [5] G. Cao and P. Schlottmann, *Rep. Prog. Phys.* **81**, 042502 (2018).
- [6] B. J. Kim, H. Jin, S. J. Moon, J.-Y. Kim, B.-G. Park, C. S. Leem, J. Yu, T. W. Noh, C. Kim, S.-J. Oh, J.-H. Park, V. Durairaj, G. Cao, and E. Rotenberg, *Phys. Rev. Lett.* **101**, 076402 (2008).
- [7] J. W. Kim, Y. Choi, J. Kim, J. F. Mitchell, G. Jackeli, M. Daghofer, J. van den Brink, G. Khaliullin, and B. J. Kim, *Phys. Rev. Lett.* **109**, 037204 (2012).
- [8] Y. Singh and P. Gegenwart, *Phys. Rev. B* **82**, 064412 (2010).
- [9] Y. Singh, S. Manni, J. Reuther, T. Berlijn, R. Thomale, W. Ku, S. Trebst, and P. Gegenwart, *Phys. Rev. Lett.* **108**, 127203 (2012).
- [10] A. Biffin, R. D. Johnson, S. Choi, F. Freund, S. Manni, A. Bombardi, P. Manuel, P. Gegenwart, and R. Coldea, *Phys. Rev. B* **90**, 205116 (2014).
- [11] T. Takayama, A. Kato, R. Dinnebier, J. Nuss, H. Kono, L. S. I. Veiga, G. Fabbris, D. Haskel, and H. Takagi, *Phys. Rev. Lett.* **114**, 077202 (2015).
- [12] K. A. Modic, T. E. Smidt, I. Kimchi, N. P. Breznay, A. Biffin, S. Choi, R. D. Johnson, R. Coldea, P. Watkins-Curry, G. T. McCandless, J. Y. Chan, F. Gandara, Z. Islam, A. Vishwanath, A. Shekhter, R. D. McDonald, and J. G. Analytis, *Nat. Commun.* **5**, 4203 (2014).
- [13] Y. Okamoto, M. Nohara, H. Aruga-Katori, and H. Takagi, *Phys. Rev. Lett.* **99**, 137207 (2007).
- [14] G. Jackeli and G. Khaliullin, *Phys. Rev. Lett.* **102**, 017205 (2009).
- [15] J. Chaloupka, G. Jackeli, and G. Khaliullin, *Phys. Rev. Lett.* **105**, 027204 (2010).
- [16] J. Chaloupka, G. Jackeli, and G. Khaliullin, *Phys. Rev. Lett.* **110**, 097204 (2013).
- [17] G. Khaliullin, *Phys. Rev. Lett.* **111**, 197201 (2013).
- [18] G. Cao, T. F. Qi, L. Li, J. Terzic, S. J. Yuan, L. E. DeLong, G. Murthy, and R. K. Kaul, *Phys. Rev. Lett.* **112**, 056402 (2014).
- [19] J. Terzic, H. Zheng, F. Ye, H. D. Zhao, P. Schlottmann, L. E. De Long, S. J. Yuan, and G. Cao, *Phys. Rev. B* **96**, 064436 (2017).
- [20] B. Ranjbar, E. Reynolds, P. Kayser, B. J. Kennedy, J. R. Hester, and J. A. Kimpton, *Inorg. Chem.* **54**, 10468 (2015).
- [21] T. Dey, A. Maljuk, D. V. Efremov, O. Kataeva, S. Gass, C. G. F. Blum, F. Steckel, D. Gruner, T. Ritschel, A. U. B. Wolter, and et al., *Phys. Rev. B* **93**, 014434 (2016).
- [22] B. F. Phelan, E. M. Seibel, D. Badoe, W. Xie, and R. Cava, *Solid State Commun.* **236**, 37 (2016).
- [23] Q. Chen, C. Svoboda, Q. Zheng, B. C. Sales, D. G. Mandrus, H. D. Zhou, J.-S. Zhou, D. McComb, M. Randeria, N. Trivedi, and J.-Q. Yan, *Phys. Rev. B* **96**, 144423 (2017).
- [24] L. T. Corredor, G. Aslan-Cansever, M. Sturza, K. Manna, A. Maljuk, S. Gass, T. Dey, A. U. B. Wolter, O. Kataeva, A. Zimmermann, M. Geyer, C. G. F. Blum, S. Wurmehl, and B. Büchner, *Phys. Rev. B* **95**, 064418 (2017).
- [25] F. Hammerath, R. Sarkar, S. Kamusella, C. Baines, H.-H. Klauss, T. Dey, A. Maljuk, S. Gaß, A. U. B. Wolter, H.-J. Grafe, S. Wurmehl, and B. Büchner, *Phys. Rev. B* **96**, 165108 (2017).
- [26] S. Bhowal, S. Baidya, I. Dasgupta, and T. Saha-Dasgupta, *Phys. Rev. B* **92**, 121113 (2015).
- [27] O. N. Meetei, W. S. Cole, M. Randeria, and N. Trivedi, *Phys. Rev. B* **91**, 054412 (2015).
- [28] K. Pajskr, P. Novák, V. Pokorný, J. Kolorenč, R. Arita, and J. Kuneš, *Phys. Rev. B* **93**, 035129 (2016).
- [29] A. Nag, S. Middey, S. Bhowal, S. K. Panda, R. Mathieu, J. C. Orain, F. Bert, P. Mendels, P. G. Freeman, M. Mansson, H. M. Ronnow, M. Telling, P. K. Biswas, D. Sheptyakov, S. D. Kaushik, V. Siruguri, C. Meneghini, D. D. Sarma, I. Dasgupta, and S. Ray, *Phys. Rev. Lett.* **116**, 097205 (2016).
- [30] A. J. Kim, H. O. Jeschke, P. Werner, and R. Valentí, *Phys. Rev. Lett.* **118**, 086401 (2017).
- [31] C. Svoboda, M. Randeria, and N. Trivedi, *Phys. Rev. B* **95**, 014409 (2017).
- [32] C. Golze, A. Alfonsov, R. Klingeler, B. Büchner, V. Kataev, C. Mennerich, H.-H. Klauss, M. Goiran, J.-M. Broto, H. Rakoto, and et al., *Phys. Rev. B* **73**, 224403 (2006).
- [33] A. Abragam and B. Bleaney, *Electron Paramagnetic Resonance of Transition Ions*, International Series of Monographs on Physics (Oxford university, New York, 2012).
- [34] T. Chang, D. Foster, and A. Kahn, *J. Res. Bur. Stand.* **83**, 133 (1978).
- [35] T. Chang and A. H. Kahn, *Standard Reference Materials : Electron Paramagnetic Resonance Intensity Standard : SRM 2601; description and use*, NBS/NIST Special Publications, Vol. 26-59 (National Bureau of Standards, Washington, DC, 1978).
- [36] D. L. Huber, *Phys. Rev. B* **6**, 3180 (1972).
- [37] D. L. Huber and M. S. Seehra, *J. Phys. Chem. Solids* **36**, 723 (1975).
- [38] J.-H. Choy, D.-K. Kim, S.-H. Hwang, G. Demazeau, and D.-Y. Jung, *J. Am. Chem. Soc.* **117**, 8557 (1995).
- [39] J. P. Clancy, N. Chen, C. Y. Kim, W. F. Chen, K. W. Plumb, B. C. Jeon, T. W. Noh, and Y.-J. Kim, *Phys. Rev. B* **86**, 195131 (2012).
- [40] G. C. Allen, G. A. M. El-Sharkawy, and K. D. Warren, *Inorg. Chem.* **11**, 51 (1972).
- [41] R. H. Magnuson, *Inorg. Chem.* **23**, 387 (1984).
- [42] P. A. Reynolds, C. D. Delfs, B. N. Figgis, M. J. Hender-

- son, B. Moubaraki, and K. S. Murray, *J. Chem. Soc., Dalton Trans.*, 2309 (1992).
- [43] N. A. Bogdanov, V. M. Katukuri, J. Romhanyi, V. Yushankhai, V. Kataev, B. Buechner, J. van den Brink, and L. Hozoi, *Nat. Commun.* **6**, 7306 (2015).
- [44] J. H. E. Griffiths and J. Owen, *Proc. Royal Soc. A* **226**, 96 (1954).
- [45] O. F. Schirmer, A. Forster, H. Hesse, M. Wohlecke, and S. Kapphan, *J. Phys. C: Solid State Phys.* **17**, 1321 (1984).
- [46] M. V. Ganduglia-Pirovano, A. Hofmann, and J. Sauer, *Surf. Sci. Rep.* **62**, 219 (2007).
- [47] M. Iakovleva, E. Vavilova, H.-J. Grafe, S. Zimmermann, A. Alfonsov, H. Luetkens, H.-H. Klauss, A. Maljuk, S. Wurmehl, B. Büchner, and V. Kataev, *Phys. Rev. B* **91**, 144419 (2015).
- [48] X. Ou, Z. Li, F. Fan, H. Wang, and H. Wu, *Sci. Rep.* **4**, 7542 (2014).
- [49] S. Kanungo, B. Yan, C. Felser, and M. Jansen, *Phys. Rev. B* **93**, 161116 (2016).
- [50] See the attached Supplemental Material for the statistical analysis of the distribution of magnetic centers on a simple- and double-perovskite lattice.

Unraveling the nature of magnetism of the $5d^4$ double perovskite Ba_2YIrO_6

Supplemental Information

S. Fuchs,^{1,2} T. Dey,¹ G. Aslan-Cansever,^{1,2} A. Maljuk,¹ S. Wurmehl,¹ B. Büchner,^{1,2} and V. Kataev¹

¹Leibniz Institute for Solid State and Materials Research IFW Dresden, D-01171 Dresden, Germany

²Institut für Festkörper- und Materialphysik, Technische Universität Dresden, D-01062 Dresden, Germany

STATISTICAL ANALYSIS OF THE DISTRIBUTION OF MAGNETIC CENTERS

Numerical simulations

For a better understanding of the experimental results we have performed numerical simulations of the statistical distribution of paramagnetic centers in Ba_2YIrO_6 as a function of their concentration n and analyzed the dependence of the average distance between the defects on n and the formation of clusters and the evolution of their size as a function of n . A cluster is defined as a group of magnetic defects interacting over a given distance, and the cluster size means the number of such defects in the group.

The double perovskite (DP) structure $\text{A}_2\text{BB}'\text{O}_6$ can be understood as the superposition of two interpenetrating simple perovskite (SP) lattices ABO_3 and $\text{AB}'\text{O}_3$, i.e., if $\text{B}=\text{B}'$ it reduces to the perovskite lattice ABO_3 . The majority of paramagnetic species giving rise to magnetism of Ba_2YIrO_6 were identified in the ESR experiments with Ir^{4+} ($S = 1/2$) and Ir^{6+} ($S = 3/2$) centers. If these centers reside exclusively on the $\text{B}' = \text{Ir}$ sites of the DP lattice then the shortest exchange interaction path p_1 would involve two oxygen bridges $\text{Ir}-\text{O}-\text{O}-\text{Ir}$, and the next one p_2 could involve the Y^{3+} nonmagnetic site, $\text{Ir}-\text{O}-\text{Y}-\text{O}-\text{Ir}$ [1]. If, however, these centers may occupy both B' and B sites then the shortest exchange path p_0 would be between the two neighboring corner-sharing octahedra $\text{B}'\text{O}_6$ and BO_6 . In this case, the problem reduces to the one on the SP lattice. For completeness, one can also define a direct geometrical distance d between two spin centers which could be relevant for dipole-dipole interaction.

The algorithm of the simulation program includes the random filling up with a given percentage of defects n an N^3 cubic lattice with the edge length of $N = 51$ sites. The lattice could be either DP or SP where the average smallest distance D_{av} between the defects in the relevant units p_i ($i = 0, 1, 2$) or d is calculated in the next step. To improve the statistics, the simulation is repeated several times and the results are averaged.

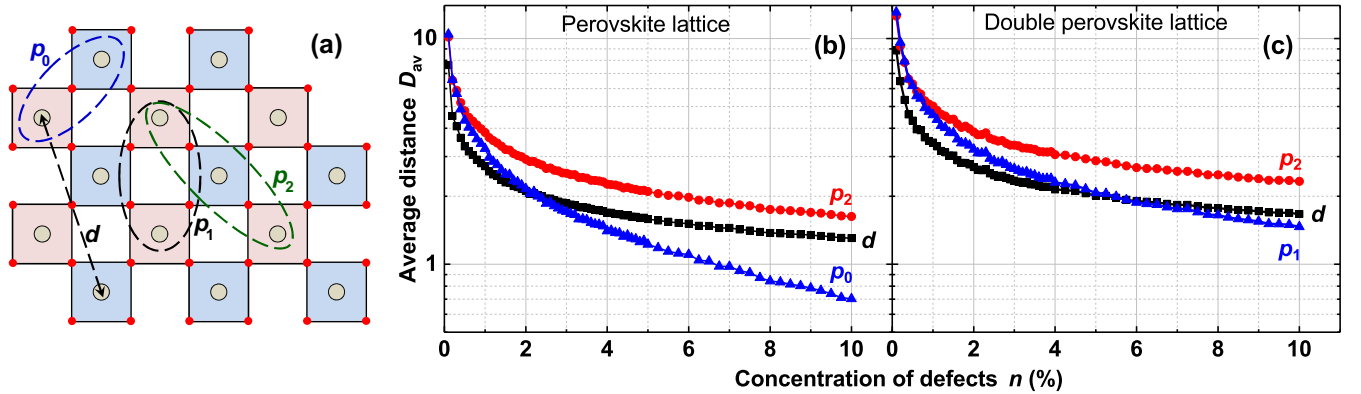


FIG. S1: (a) Definition of exchange path units in the DP lattice $\text{A}_2\text{BB}'\text{O}_6$: between nearest corner shared octahedra $\text{B}'\text{O}_6$ and BO_6 – p_0 ; via two oxygen bridges $\text{B}'-\text{O}-\text{O}-\text{B}'$ – p_1 ; via the bridge $\text{B}'-\text{O}-\text{B}-\text{O}-\text{B}'$ – p_2 ; d is the geometrical distance between two selected sites; Average distance between the defects in an SP (b) and DP (c) lattice as a function of the defect concentration n for four differently defined distance units p_0 , p_1 , p_2 and d . Solid lines are guide for the eye. (see the text)

In Fig. S1 the average distance D_{av} between the defects in the above introduced definitions of the distance units is plotted as a function of the defect concentration n for SP and DP lattices. As expected, D_{av} shrinks with increasing n . Interestingly, it drops down very fast in the range $0 < n \lesssim 2\%$ and then decreases smoothly further for higher n . In the SP lattice with 2% of defects, D_{av} amounts to two shortest exchange path units p_0 , whereas in the DP lattice with the shortest exchange path p_1 , one reaches $D_{\text{av}} = 2p_1$ at $n = 5.5\%$ only. To illustrate the distribution of the defect centers, we show in Fig. S2 examples of the stochastic filling of an SP lattice with defects for three values of n .

Defect centers which generally can occur at every site are visualized as small colored spheres. Spheres with the same color are connected via exchange path of the same length. The number of particles with shorter interaction lengths rapidly grows with n , as expected.

Fig. S3 visualizes the formation of clusters on the SP lattice with increasing the concentration of defects n . Defects are depicted as small differently colored spheres. Defects belonging to the same cluster have the same color. The color itself has no special meaning and is chosen randomly for different clusters. While at the smallest concentration of 2% there are practically no clusters formed, they become appreciable at $n = 4\%$, and at $n = 10\%$ almost all defects are coupled in one cluster.

Fig. S4 presents the results of the cluster analysis where several relevant quantities obtained from the simulations are plotted as a function of the concentration of the paramagnetic centers n . The distance between the neighboring centers in a cluster is defined in exchange path units p_0 , p_1 and p_2 , respectively. In panel (a) the number of clusters in the lattice is normalized to the number of total lattice sites available for the defects $N_{\text{cl}}^{\text{norm}}$. At small n , the number of defects increases without forming any clusters. At a certain concentration, the clusters begin to form and their number grows with further increasing n . However, above some specific concentration of defects, which depends on

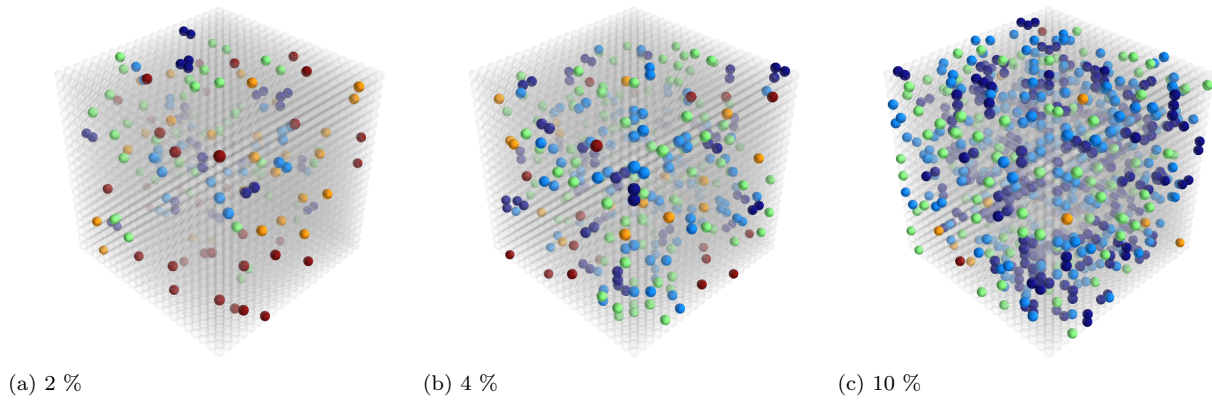


FIG. S2: Examples of the distribution of defects (colored spheres) on an SP lattice with the edge length of $N = 21$ sites for three selected concentrations n . The color identifies the defects having the same distance to the nearest neighbor defined in the units of the exchange path p_0 : dark blue $= p_0$; light blue $= 2p_0$; green $= 3p_0$; orange $= 4p_0$, and red $\geq 5p_0$. (see the text)

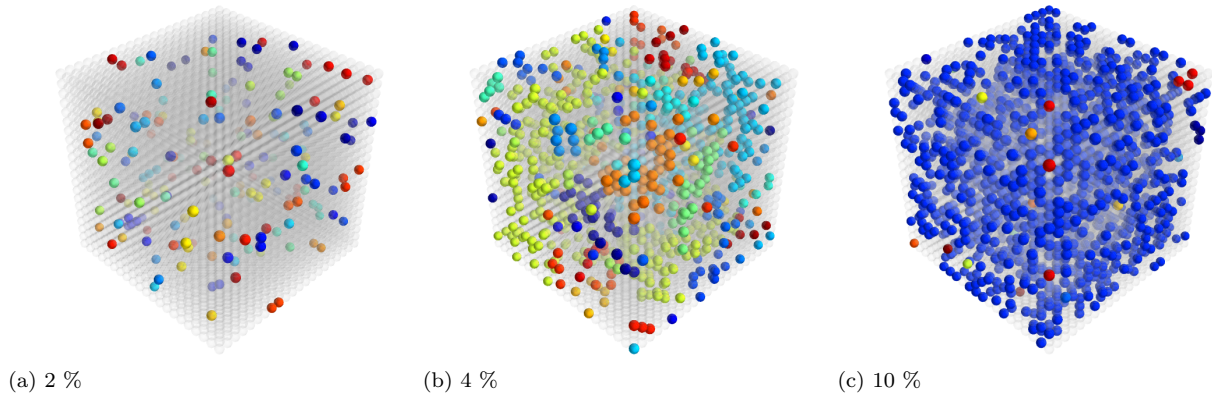


FIG. S3: Examples of the clustering of defects (colored spheres) on an SP lattice with the edge length of $N = 21$ sites with increasing their concentration n . The defects are connected in a cluster by the maximum exchange path length of $2p_0$. Defects belonging to the same cluster have the same color. (a) $n = 2\%$, practically all defects are independent; (b) $n = 4\%$, defects are coupled in mid-size clusters; (c) $n = 10\%$, practically all defects belong to the same cluster.

the chosen interaction distance between the defects in the cluster (p_0 , $2p_0$, p_1 , or $2p_1$) and the type of the lattice (SP or DP), the number of clusters decreases since more and more defects are joining the same cluster. Panel (b) depicts the concentration dependence of the average cluster size S_{av} . Remarkably, S_{av} grows exponentially with n for all types of interaction distances. Panel (c) shows the dependence on n of the size of the largest cluster normalized to the number of all defects S_{max}^{norm} . The value of 1 means that all defects belong to one cluster. It is instructive to define a threshold concentration n_{th} at which $S_{max}^{norm} = 0.5$ meaning that one half of the defects belongs to the largest cluster. The average cluster size at the concentration n_{th} amounts to $\approx 8(\pm 1)$ irrespective of the chosen interaction distance [Fig. S4(b)].

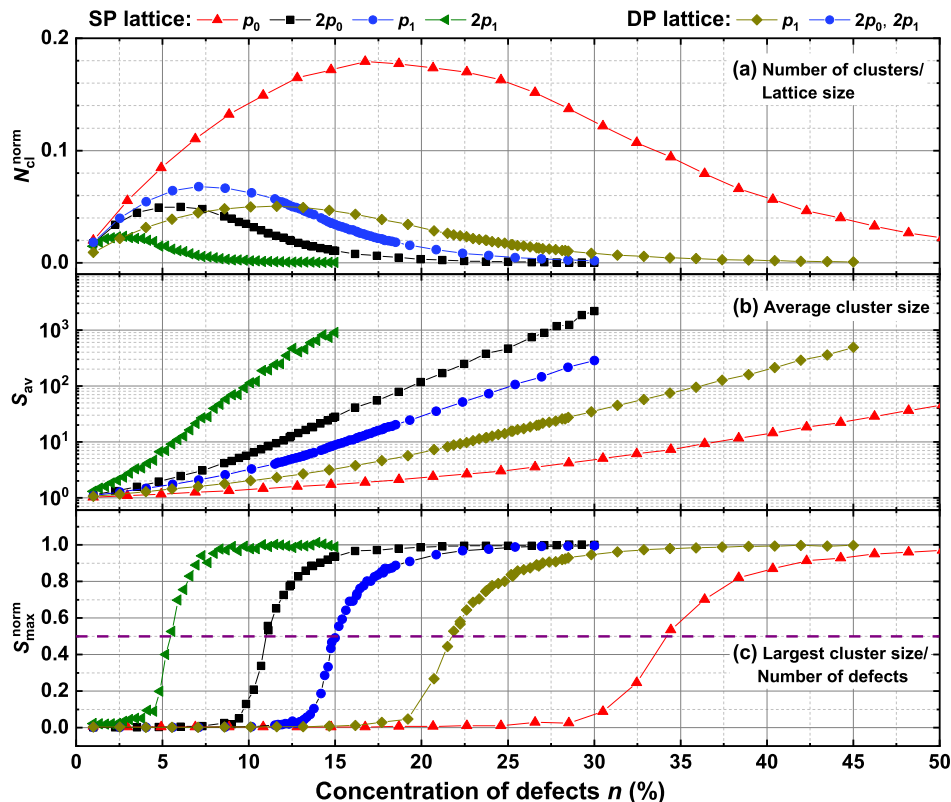


FIG. S4: Results of the cluster analysis for SP and DP lattice for three differently defined distance units p_0 , p_1 and p_2 . Dependence on the defect concentration n of: (a) number of clusters normalized to the number of total lattice sites N_{cl}^{norm} ; (b) average cluster size S_{av} ; (c) size of the largest cluster normalized to the number of all defects S_{max}^{norm} . Horizontal dashed line in (c) indicates the level at which one half of all defects in the lattice belongs to the largest cluster. The corresponding threshold concentration n_{th} where the line intersects the curves depends on the distance between the centers in the cluster. Solid lines are guides for the eye. (see the text)

Discussion

According to the above analysis, the full percolation in the DP lattice is achieved at the concentration of defects in the range 20 - 30% depending on the length of the chosen exchange path p_1 or $2p_1$ [Fig. S4(c)]. For the case of the SP lattice it reduces to 8 - 20%, respectively. Since the samples studied in the present work do not order magnetically and the concentration of magnetic centers is relatively small ($\sim 4\%$), the situation is far away from the full percolation. Still, magnetic correlations are evident from susceptibility and ESR data. This supports theoretical ideas of long-range character of superexchange in the $5d$ DP compounds [1, 2] whereas some antisite $Y \leftrightarrow Ir$ disorder might also play a role [3]. Significant antisite disorder which effectively reduces the interactions between magnetic centers to the case of the SP lattice with shorter exchange paths might help to rationalize the occurrence of magnetic order in "stronger magnetic" samples. However, at least in the case of "weaker magnetic" samples studied in the present work it remains an open question if one could treat Ba_2YIrO_6 as a simple perovskite.

-
- [1] S. Kanungo, B. Yan, C. Felser, and M. Jansen, *Phys. Rev. B* **93**, 161116 (2016).
 - [2] X. Ou, Z. Li, F. Fan, H. Wang, and H. Wu, *Sci. Rep.* **4** (2014), 10.1038/srep07542.
 - [3] Q. Chen, C. Svoboda, Q. Zheng, B. C. Sales, D. G. Mandrus, H. D. Zhou, J.-S. Zhou, D. McComb, M. Randeria, N. Trivedi, and J.-Q. Yan, *Phys. Rev. B* **96**, 144423 (2017).